Modeling and Design of a Transcutaneous Resonant Capacitive Power Transfer Link for Biomedical Implants

Chunwei Cai, *Member, IEEE*, Tian Chen, Xiuyun Ren, Yujie Jiao, Xichen Liu, *Student Member, IEEE*, Chenghao Li, *Student Member, IEEE*, Jinpeng Yu, *Senior Member, IEEE*, and Shuai Wu, *Member, IEEE*

***Abstract*—This article proposes a transcutaneous resonant capacitive power transfer link for biomedical implants using parallel thin-film electrodes as coupling plates. First, the practical multilayer tissue circuit model is obtained by tissue dielectric properties and current path. Analysis is presented to identify the influencing factors of loss mechanisms on power transfer efficiency (PTE) and power delivered to the load (PDL). Then, an asymmetric insulation layer coupler is proposed to reduce losses. The parameters of this design are obtained from the finite-element method for maximum PTE and high PDL. Moreover, the safety assessment and power transfer strategies are performed according to the IEEE C95.1 guideline; 90.73 mW of PDL is safely received at 47.02% PTE. Finally, two sets of comparative experiments are conducted at 6.78-MHz operating frequency using pork as the medium, evaluating the performance of symmetric insulation layer ($t_2 = 0.015$ mm) and asymmetric insulation layer coupler ($t_2 = 0.15$ mm). The experimental results show good agreement with the analytical and simulation results; the asymmetric insulation layer compared with the symmetry insulation layer improves efficiency by 8.9%.**

***Index Terms*—Biomedical implants, capacitive links, capacitive power transfer (CPT).**

I. Introduction

IMPLANTABLE biomedical devices in the human body are extensively utilized in medical diagnostics, treatment, monitoring, and biological research. The required power for these devices varies from a few microwatts to several watts, depending on the application scenario [1], [2], [3], [4], [5], [6], [7], [8]. Presently, low-power implants, such as pacemakers, rely on batteries predominantly, necessitating periodic surgical interventions for replacement due to their limited battery capacity [9]. Higher power implants, such as artificial hearts, commonly derive power through wire penetrating the skin, introducing a potential risk of infection. Wireless power transfer (WPT) technology is the preferred approach for energy supply in implantable devices due to its sustainability and safety.

Different WPT technologies have been investigated in current research, including ultrasonics [10], antennas [11], inductive power transfer (IPT), capacitive power transfer (CPT), and volume conduction (VC) methods. Among these, IPT is considered the most developed method for wireless charging and has been extensively researched in implants, such as artificial hearts, pacemakers, and neurostimulators, ranging from microwatts to milliwatts [12], [13], [14]. However, there are two main limitations to IPT. First, high eddy loss is inevitable, which makes it difficult to integrate into implants with metallic components. Second, the electromagnetic interference (EMI) may affect the proper functioning of the implant devices. Implants powered by ultrasonics or antennas at a depth of a few centimeters often face the problem that their low power transfer efficiency (PTE) and power delivered to the load (PDL) make it difficult to satisfy the power requirements of some implanted devices.

VC has been extensively studied in human body communication [15], [16], and recently, it has been reported in the WPT of implantable devices [17], [18]. VC and CPT are very similar in that they both transmit energy through conduction and displacement current between tissues. The difference is that VC is suitable for providing energy for deep low-power implants and has a larger energy transmitter (Tx). Minguillon et al. [19] employed a long threadlike implant as the voltage pick-up electrode and human experiments were conducted. Unfortunately, the exposed electrodes on the receiving side may cause infection in human tissues. To address this problem, literature [20] investigated the vertical four-plate structure with the insulation layer. However, the validation was done using NaCl solution, which did not take capacitance characteristics into consideration.

CPT, a novel optional WPT method, employs two pairs of biocompatible insulated plates for energy transfer. The receiving plates are usually designed to be thin and flexible to meet

Received 28 June 2024; revised 24 August 2024; accepted 7 October 2024. Date of publication 10 October 2024; date of current version 18 December 2024. This work was supported in part by the National Natural Science Foundation of China under Grant 52401406, in part by the Taishan Scholars of Shandong Province under Grant tsqnz20240801, and in part by the Major Scientific and Technological Innovation Project of Shandong Province of China under Grant 2022ZLGX04. Recommended for publication by Associate Editor A. Kuperman. *(Corresponding author: Shuai Wu.)*

Chunwei Cai, Tian Chen, Xiuyun Ren, Yujie Jiao, Xichen Liu, Chenghao Li, and Shuai Wu are with the School of New Energy, Harbin Institute of Technology, Weihai 264209, China, and also with the Key Laboratory of Cross-Domain Synergy and Comprehensive Support for Unmanned Marine Systems, Ministry of Industry and Information Technology, Weihai 264209, China (e-mail: caichunwei@hit.edu.cn; 22s130575@stu.hit.edu.cn; renxiuyun@hit.edu.cn; 23s130529@stu.hit.edu.cn; 21s030155@stu.hit.edu.cn; 23b906007@stu.hit.edu.cn; wushuai@hit.edu.cn).

Jinpeng Yu is with the School of Automation, Qingdao University, Qingdao 266071, China (e-mail: yjp1109@qdu.edu.cn).

Color versions of one or more figures in this article are available at https://doi.org/10.1109/TPEL.2024.3477615.

Digital Object Identifier 10.1109/TPEL.2024.3477615

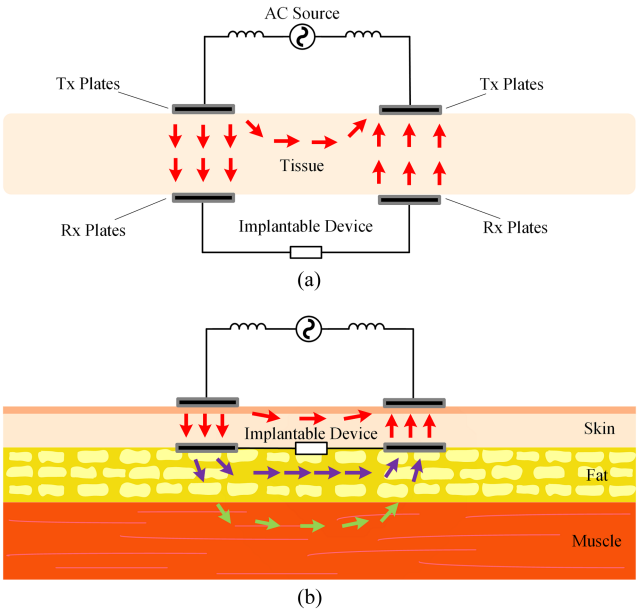

Fig. 1. (a) Single-layer tissue model in past resonant CPT. (b) Multilayer tissue model analyzed in this work.

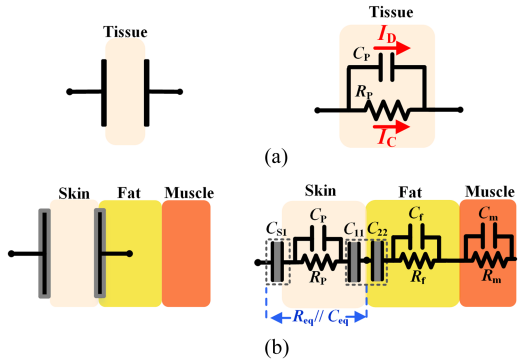

Fig. 2. (a) Single-layer tissue with one pair of uncoated plates (left) and its circuit model (right). (b) Multilayer tissue with one pair of coated plates (left) and its circuit model (right).

subcutaneous implantation requirements. To improve PTE and PDL by reducing the impedance of the insulation layer capacitor in the link, the resonant circuit and the nonresonant circuit are typically used. The resonant circuit (<20 MHz) enhances the energy transfer capacity by using series inductors, while the nonresonant (>100 MHz) circuit raises the frequency to reduce the impedance of CPT link [21]. Tamura et al. [22], [23], [24], [25] followed their circuit model in fresh water and developed a six-impedance transformation to a two-port Π circuit model of human tissue and then investigated nonresonant CPT for intravascular implant and pacemaker. However, the rectifier of nonresonant CPT reduces its ac–dc PTE above 100 MHz. For resonant CPT, Erfani et al. [26] and [27] have introduced and validated a six-impedance model for single-layer tissue. Literature [28] analyzed nonideal conditions and confirmed insensitivity to misalignments and bending of the plates caused by human motion for resonant CPT. Literature [29] proposed an algorithmic optimization design for resonant CPT as well as nonresonant CPT, and experimental validation was done by single-layer beef.

To minimize the detrimental effect of high fat layer impedance on energy transfer link, subcutaneous implantation (between skin and fat layer) of flexible and thin electrodes is a common option to ensure high PTE and PDL for resonant CPT. Long-term subcutaneous implantation has been validated to be safe by a long-term in vivo experiment [38] as well as practical applications [30]. However, current resonant CPT studies focus on the impact of the tissue between insulated Tx and receiver (Rx) plates, as shown in Fig. 1(a). In fact, there are multiple layers of tissue behind the plates, as shown in Fig. 1(b); some nonresonant CPTs consider the real implantation environment, but the impact of these tissues on the CPT link has not been investigated. Therefore, additional research is required to investigate the impact of multilayer tissue on resonant CPT energy transfer and design coupling link that mitigate adverse effects.

The main contributions of this article are summarized as follows.

1) The effect of frequency-dominated tissue dielectric properties on the resonant CPT link is analyzed, and the two-port T impedance circuit model of multilayer tissue in the resonant CPT link is proposed to analyze the power distribution as well as the loss mechanism.
2) The design of a practical asymmetric insulation implants aiming for high PTE and PDL is detailed, and the effects of operating frequency, compensation, and insulation on the link are illustrated.
3) Strategies to improve PDL, misalignment tolerance, and implant miniaturization are discussed under the IEEE C95.1 guideline.

The rest of this article is organized as follows. Section II analyzes the dielectric properties of tissue layers and derives the circuit topology. Section III designs the coupler and analyzes the energy transfer capability. In Section IV, safety standards are discussed, and power transfer strategies are evaluated. In Section V, two sets of comparative CPT experiments are conducted, and the experimental results are compared with the analytical and simulation results. Finally, Section VI concludes this article.

II. Dielectric Properties and Circuit Models of Biological Tissues in the CPT Link

A. Tissue Model in the CPT Link

The human body primarily comprises skin (∼16% in weight), fat (10%–30% in weight), and muscle (30%–50% in weight), collectively forming a multilayer tissue. Each layer of tissue, as dielectric material, exhibits both capacitance and conductivity. It can be modeled as a pair of parallel resistance and capacitance, as shown in Fig. 2(a) [27]. The capacitor C_p allows for displacement current I_D without losses, while the resistance R_p allows for conducting current I_C, causing thermal effects in the tissue, which are the main losses in the link. The relative

permittivity $\varepsilon_{\mathrm{r}}(\omega)$ and conductivity $\sigma_{\mathrm{T}}(\omega)$ are functions dominated by three main relaxation regions as frequency changes. Obtained by Gabriel's Cole–Cole model [31], [32], [33], the complex relative permittivity of the tissue ε^* can be shown by

$$\varepsilon^* = \varepsilon_\infty + \sum_{n=1}^{4} \frac{\Delta\varepsilon_n}{1+(j\omega\tau)^{(1-\alpha_n)}} + \frac{\sigma_{\mathrm{i}}}{j\omega\varepsilon_0} \tag{1}$$

where ε_∞ is the permittivity at the frequency much higher than the first relaxation resonance, $\Delta\varepsilon_n$ is the magnitude of the dispersion for the nth relaxation region, τ is the time constant of the tissue, σ_{i} is the static ionic conductivity, ε_0 is the vacuum permittivity, and α_{n} is the distribution parameter. Relative permittivity and conductivity can be shown as

$$\varepsilon_{\mathrm{r}}(\omega) = \mathrm{real}(\varepsilon^*) \tag{2}$$

$$\sigma_{\mathrm{T}}(\omega) = -2\pi f\varepsilon_0 \cdot \mathrm{imag}(\varepsilon^*). \tag{3}$$

Multilayer tissue can be simplified into three layers, representing the skin layer, the fat layer, and the muscle layer, as shown in Fig. 2(b). Film plates with insulation layers are placed in parallel on both the sides of the skin layer, and the Rx electrode plates form capacitance C_{11} and C_{22} with the skin and fat, respectively. The Tx electrode plates form capacitance C_{S1} with the surface of skin. The use of insulating material for wrapping avoids the risk of potential infection while allowing the thin insulating layer to form capacitances C_{S1} and C_1 that dominate the equivalent capacitance C_{eq}.

The tissue dissipation factor $tg\delta(\omega)$, a function of frequency, represents the ratio of conduction current to displacement current and indicates the rate of energy loss, which can be expressed as

$$tg\delta(\omega) = \frac{I_{\mathrm{C}}}{I_{\mathrm{D}}} = \frac{\sigma_{\mathrm{T}}(\omega)}{\omega\varepsilon_0\varepsilon_{\mathrm{r}}(\omega)}. \tag{4}$$

To improve PTE, it is crucial to choose a working frequency with the low tissue dissipation factor. Fig. 3 shows the relative permittivity, conductivity, and tissue dissipation factor for skin, fat, and muscle at operating frequencies ranging from 10 to 10^{10} Hz. As can be seen, in the frequency range of 100 kHz to 40 MHz, the tissue dissipation factor of skin, which is the primary medium for energy transfer, increases with frequency. In addition, fat and muscle tissue exhibit a higher energy loss rate than skin. To comply with the ITU-R regulations on radio frequency (RF) bands, 6.78 MHz in the industrial scientific medical (ISM) band is chosen as the operating frequency, considering of the dissipation factor $tg\delta(\omega)$.

B. Transcutaneous CPT Link Model

When two pairs of plates with insulation layers contact human skin, capacitive coupling is formed between the plates. This allows energy to be transferred by currents (conduction and displacement currents), which are geometrically segmented according to the different tissue layers of human body as well as the path of the currents and are modeled with both the transverse and longitudinal impedances. As shown in Fig. 4(a), Z_{ij} characterizes its transverse impedance, Z_j characterizes its

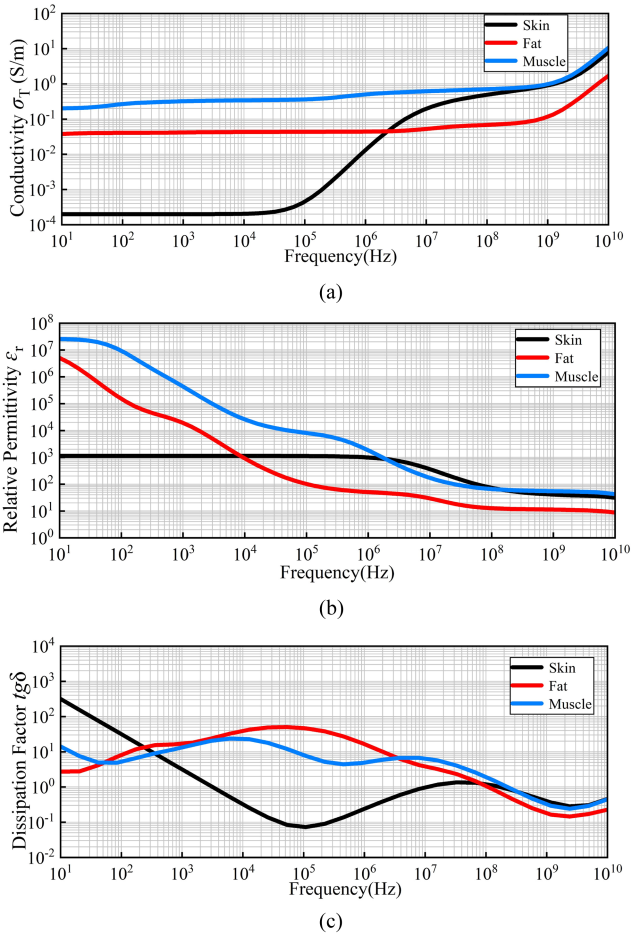

Fig. 3. (a) Conductivity, (b) relative permittivity, and (c) dissipation factor as function of frequency for different tissues.

longitudinal impedance (i = 1,2,3,4; j = s, f, and m, where "s" stands for skin, "f" for fat, and "m" for muscle) and bypass impedance Z_{sf} characterizes the impedance of the current path from the side entry to the fat layer, which is usually very large. Each impedance can be modeled as a capacitor and a resistor in parallel. As the impedance of the insulation layer cannot be ignored in the resonant CPT link, the Tx insulation capacitance is expressed as $C_{\mathrm{S1,2}}$, and the Rx insulation capacitance is comprised by two parts: 1) upper insulation layer capacitance C_1 and C_3, formed between the Rx copper plate and the skin, and 2) lower insulation layer capacitance C_2 and C_4, formed between the Rx copper plates and the fat, where $C_1 = C_3$ and $C_2 = C_4$. The magnitude of these capacitances depends on the area and thickness of the insulation layers, as well as their relative dielectric constants.

The series inductors compensating the insulating layer capacitance at the Tx and Rx sides can be expressed as

$$L_{\mathrm{S1,2}} = k_1 \frac{1}{\omega^2 C_{\mathrm{S1,2}}} \tag{5}$$

$$L_{1,2} = k_2 \frac{1}{\omega^2 C_{11,33}} \tag{6}$$

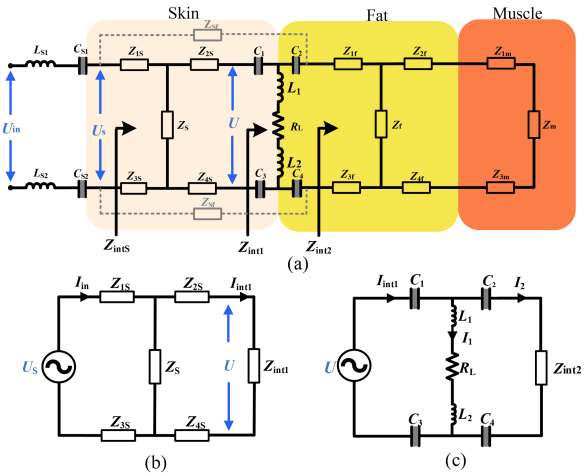

Fig. 4. (a) Transcutaneous CPT link model. (b) and (c) Simplified equivalent circuits.

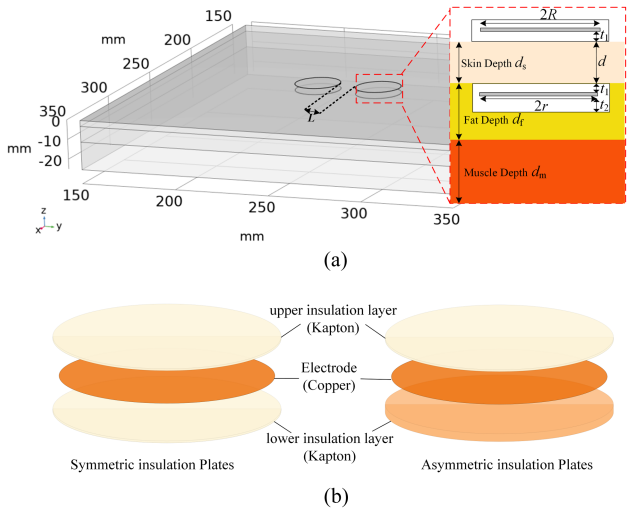

Fig. 5. (a) Schematic of the geometric model in COMSOL. (b) Exploded view of symmetric and asymmetric insulation Rx plate.

where k_1 and k_2 represent the compensation coefficients, and the skin surface voltage U_S can be expressed as

$$U_S = \frac{Z_{ints}}{2(k_1-1)j\omega L_{S1} + Z_{ints}} U_{in}. \tag{7}$$

To keep U_S from being affected by the impedance of the back stage, k_1 presets to "1" to maintain $U_S = U_{in}$. Then, the circuit topology of Fig. 4(a) is divided into two parts: the skin tissue with input impedance Z_{int1} shown in Fig. 4(b) and the Rx plates with the input impedance Z_{int2} shown in Fig. 4(c). For further analyzing the circuit working principle, we calculate the circuit through the Kirchhoff voltage law (KVL) for Fig. 4(b) and (c).

The KVL equation of Fig. 4(b) indicates that

$$U_{Z_s}\left(\frac{1}{Z_s}+\frac{1}{Z_1}+\frac{1}{Z_2}\right) = \frac{U_s}{Z_1} \tag{8}$$

where $Z_1 = Z_{1S}+Z_{3S}$ and $Z_2 = Z_{2S}+ Z_{int1}+ Z_{4S}$. According to (8), I_{in} and I_{int1} are determined to be

$$I_{int1} = \frac{U_S}{Z_1 Z_2 (1/Z_1 + 1/Z_s + 1/Z_2)} \tag{9}$$

$$I_{in} = \frac{U_s}{Z_1\,(1/Z_1 + 1/Z_s + 1/Z_2)}\left(\frac{1}{Z_2}+\frac{1}{Z_S}\right). \tag{10}$$

The equation that describes the relationship between I_1 and I_2 in Fig. 4(c) can be expressed as follows:

$$I_1(j\omega L_1 + j\omega L_2 + R_L) = I_2\left(\frac{1}{j\omega C_2}+\frac{1}{j\omega C_4}+Z_{int2}\right) \tag{11}$$

where I_1 and I_2 represent the current flowing into the load and the backside tissue, respectively. The ratio of current I_1 to current I_2 and the currents can be expressed as follows:

$$\begin{cases} \alpha = \frac{I_1}{I_2} = \frac{Z_{int2}+2/j\omega C_2}{R_L - 2k_2/j\omega C_1} \\ I_1 = \frac{\alpha}{1+\alpha} I_{int1} \\ I_2 = \frac{1}{1+\alpha} I_{int1}. \end{cases} \tag{12}$$

Three mechanisms of losses that contribute to PTE degradation can be sorted out from the above analysis, namely, the skin loss P_{loss1} caused by the impedance $Z_{1,2,3,4}$ and Z_S, the backside losses P_{loss2} caused by Z_{int2}, and other losses P_{loss3} caused by insulation dielectric loss and parasitic resistance of the inductors. P_{loss1} and P_{loss2} can be expressed as follows:

$$\begin{cases} P_{loss1} = \mathrm{Re}[I_{in}Z_1(I_{in})^* + I_{int1}(Z_{2S}+Z_{4S})(I_{int1})^* \\ \quad + (I_{in}-I_{int1})Z_S(I_{in}-I_{int1})^*] \\ P_{loss2} = \mathrm{Re}(I_2 Z_{int2} I_2^*). \end{cases} \tag{13}$$

Then, PDL and PTE can be determined as

$$\begin{cases} \mathrm{PDL} = I_1^2 \cdot R_L \\ P_{in} = \mathrm{real}(U_{in} \cdot I_{in}^*) \\ \mathrm{PTE} = \mathrm{PDL}/P_{in} \times 100\%. \end{cases} \tag{14}$$

Equations (13) and (14) illustrate the losses, PTE, and PDL as a function of the input voltage U_{in}, human tissue impedance, load R_L, compensation coefficients k_2, and insulation layer capacitance. Design of the coupler is required to reduce tissue losses and enable a greater portion of the input current flowing into the upper insulation layer to be directed through the load, rather than passing through lower insulation layer to the backside, which will enhance PTE.

III. Insulated Capacitive Coupler Design and Simulation Analysis

The previous section has modeled the circuit and analyzed the factors influencing PTE and PDL. In this section, the parameters of the capacitive coupler are designed, and energy transfer capability is assessed.

The simulation model is setup in COMSOL, which is calculated by the electrical circuit and current interfaces of the ac–dc module in Fig. 5(a). The Kapton film, due to its biocompatibility, is coated to the copper plates of 400 mm^2 in area ($R = r =$ 11.28 mm) and 0.01 mm in thickness. The polar plates are designed to be circular, which allows for a more even dispersion of stress in the surrounding tissue, reducing the risk of tissue damage. The thickness of the insulation layers of the Tx plates

TABLE I
MODEL GEOMETRIC PARAMETER VALUE

Parameter	Value	Parameter	Value
d_s	3 mm	d	3 mm
d_f	8 mm	t_1	0.005–0.30 mm (Kapton)
d_m	7 mm	t_2	0.015–0.30 mm (Kapton)
f	6.78 MHz	R	11.28 mm
L	10–100 mm	r	11.28 mm

TABLE II
DIELECTRIC PROPERTIES OF MODELED TISSUES AT THE FREQUENCY OF 6.78 MHZ [31], [32], [33]

Tissues	Relative permittivity	Conductivity (S/m)
Skin	478.41	0.147
Fat	34.98	0.049
Muscle	233.27	0.602

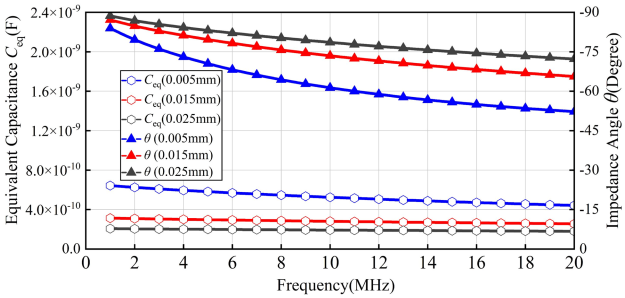

Fig. 6. Simulated equivalent capacitance and impedance angle of parallel plates with three different upper insulation layer thicknesses t_1.

and the upper insulating layer of Rx plates is set to t_1, and the thickness of the lower insulating layer of the Rx plates is set to t_2. L represents the Tx edge-to-edge separation, d represents the implant depth, and R and r represent the radius of the Tx and Rx plants, respectively. The exploded view of symmetric and asymmetric insulation Rx plates is shown in Fig. 5(b). Model geometric parameters are shown in Table I. Arranged from top to bottom are skin, fat, and muscle, and their dielectric parameters are shown in Table II.

A. Design of the Upper Insulation Layer

The circuit topology of Fig. 2(b) is used to investigate a pair of parallel plates with insulating layers. The relative permittivity of human tissues is usually much higher than insulating material. For example, at 6.78 MHz, the relative permittivity of skin can be as high as 478.41, whereas for Kapton, it is only 3.4, which results in the insulation layer having a significantly smaller capacitance than the tissue capacitance within a certain thickness range, thus dominating the equivalent capacitance of parallel plates C_{eq}. Fig. 6 demonstrated the equivalent capacitance C_{eq} and impedance angle for three distinct insulating layer thicknesses t_1 (0.005, 0.015, and 0.025 mm). The decrease in relative permittivity and rise in conductivity of tissue occur at frequencies between 1 and 20 MHz, which results in a drop in the equivalent C_{eq} and the equivalent impedance angle θ. Concurrently, the impedance angle is related to the equivalent

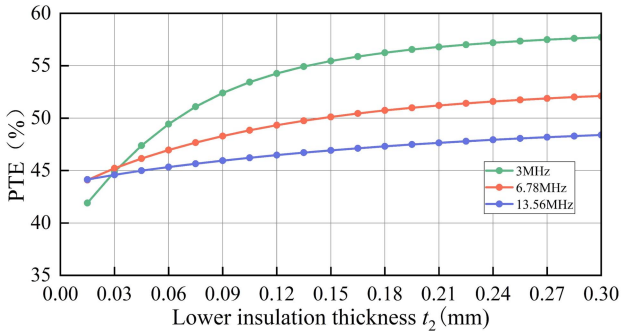

Fig. 7. Simulated PTE as a function of lower insulation layer thickness t_2 at $t_1 = 0.015$ mm.

dissipation factor between the copper plates, which is shown as

$$tg\delta_{eq} = \frac{1}{j\omega C_{eq} R_{eq}} = \frac{1}{tg|\theta|}. \tag{15}$$

The simulation results indicate that a thicker insulation layer t_1 results in a smaller $tg\delta_{eq}$; however, it should be noted that the dissipation factor in human tissue is an only frequency-dependent function, and the decrease in $tg\delta_{eq}$ for different t_1 at a fixed frequency in the aforementioned analysis is mostly due to the increase of dielectric loss in the insulating layer. Both $t_1 = 0.015$ mm and $t_1 = 0.025$ mm exhibit improved characteristics as the frequency varies, maintaining a constant equivalent capacitance and exhibiting a greater link stability. Considering the thickness as well as the dielectric properties, $t_1 = 0.015$ mm is chosen.

B. Design of the Lower Insulation Layer

The direct contact of the lower insulating layer of Rx plates with the fat layer results in a portion of the current flowing into the backside tissue layer, leading to losses. According to (12)–(14), both a larger value of α and a higher efficiency of PTE can be achieved by designing the thickness of the lower insulating layer t_2. Fig. 7 depicts the simulation results of PTE variation with insulation thickness t_2 (0.015–0.30 mm) at different frequencies. As t_2 increases, lower frequencies are more affected by the thickness of the lower insulation layer t_2, while a greater efficiency could be achieved. At 6.78 MHz, PTE increases from 44.1% ($t_2 = 0.015$ mm) to 50.12% ($t_2 = 0.15$ mm), which represents an increase of 6.02% in PTE. After t_2 reaches 0.15 mm, the rate of efficiency growth slows down. It can be assumed that most of the current flowing into the backside tissue causing backside losses is effectively isolated, and high PTE is achieved when t_2 is set as 0.15 mm.

C. Design of Compensating Inductors

For transcutaneous CPT systems, series-series (SS) and series-parallel (SP) compensation is usually utilized to improve the PTE as well as power factor of the system, and SS compensation is used in this article due to its smaller inductance. To ensure that the voltage U_s between human tissues remains limited, higher order compensation is not employed, preventing

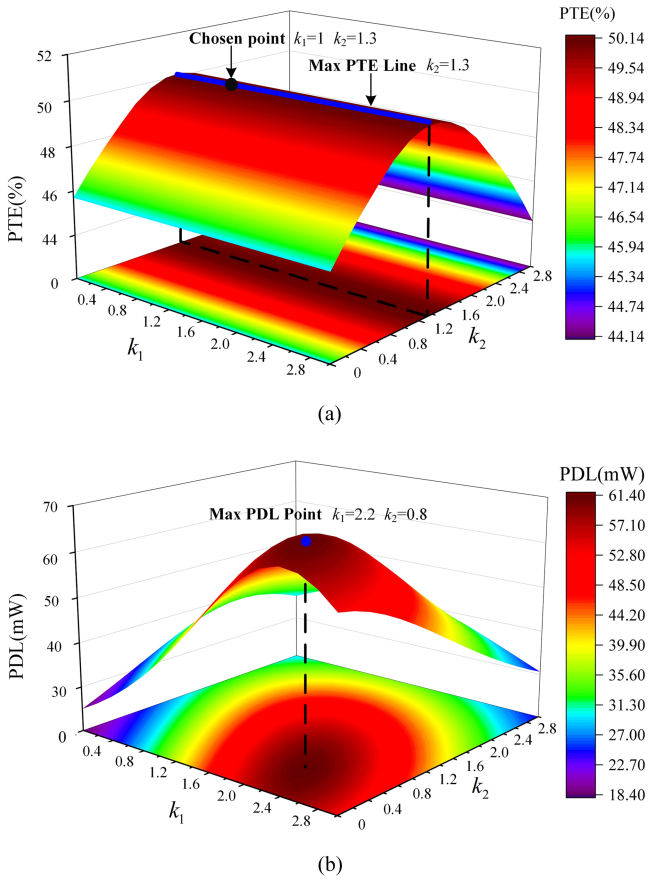

Fig. 8. (a) Simulated PTE as a function of k_1 and k_2 at 6.78 MHz. (b) Simulated PDL as a function of k_1 and k_2 at 6.78 MHz.

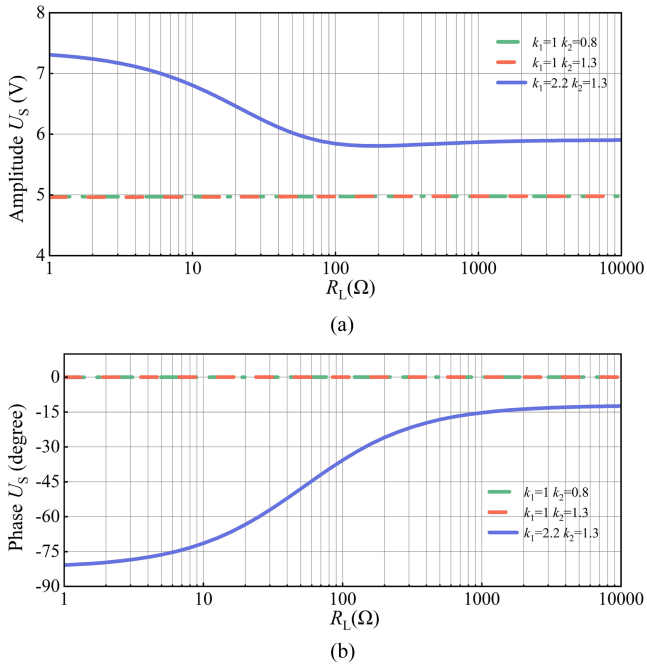

Fig. 9. (a) Simulated amplitude of skin surface voltage U_S. (b) Simulated phase of skin surface voltage U_S.

thermal and electrostimulation to the body. In order to investigate the mechanism of the influence of the Tx and Rx compensating inductors on the PTE and PDL clearly, the curves of the PTE and PDL as a function of k_1 and k_2 have been derived from simulations, as shown in Fig. 8. In these curves, each data point of PTE and PDL has been tracked to its optimum efficiency load point. In addition, the peak input voltage U_{in} has been set to 5 V.

The compensation coefficients k_1 and k_2 range from 0 to 3. The value of 0 for either k_1 or k_2 indicates no compensation at the Tx or Rx side. From Fig. 8, it can be noticed that k_1 has almost no effect on the PTE and only changes the amplitude as well as the phase of the skin surface voltage U_S, which is consistent with (7). The effect of k_1 on U_S can be further realized from Fig. 9. Compared with $k_1 = 1$, $k_1 = 2.2$ has a larger U_S amplitude, and the PDL is proportional to the square of the U_S amplitude, independent of the phase of U_S. In addition, when $k_1 = 2.2$, it can be found that the amplitude of U_S varies with the load, which leads to a load shift and makes it difficult to control the input voltage amplitude of U_{in}. Then, coefficient k_2 affects both PTE and PDL of the system, and when k_2 increases from 0 to 1.3, the Rx inductors enhance the PTE by decreasing the Rx link capacitive reactance, thus improving the PTE. The maximum PTE of 50.12% is achieved at $k_2 = 1.3$. With a further increase in k_2, the inductive reactance of the Rx link increases inversely, causing a decrease in PTE. It is worth noting that even when $k_2 = 0$, the system maintains an efficiency of above 45.7%, but this leads to a low PDL. As a result, a larger input voltage U_{in} is required to maintain the same PDL.

PTE estimates the amount of energy lost in body tissues, and the higher the PTE, the more energy can be transmitted within specific absorption rate (SAR) limits. Therefore, the maximum PTE is used as the target to design the inductors, with $k_1 = 1$ and $k_2 = 1.3$ chosen.

D. Power Transfer Capability

In this section, we evaluate the designed coupler in terms of implantation depth d, edge-to-edge separation L, and misalignment of the X-axis and the Y-axis.

Fig. 10(a) illustrates the impact of implant depth on PTE and PDL. The results indicate that the maximum PTE and PDL are obtained when located between the skin and the fat layer. PTE and PDL decrease rapidly with increasing fat thickness when the implant is in the fat layer, while both of them are less affected by the muscle tissue when the implant is implanted between the muscle layers. This suggests that implantation into the fat layer or below is a great challenge for the CPT system due to the large surface currents as well as the high dissipation factor of fat. Concurrently, the energy transfer varies significantly due to individual differences in fat thickness. The designed flexible thin-film electrode in this article (only 0.175-mm thick) allows it to be implanted between the skin and the fat layer while maintaining good biocompatibility and high PDL and PTE, making it suitable for powering mid-to-high power medical subcutaneous implants.

The results in Fig. 10(b) show that the maximum PTE and PDL are obtained when edge-to-edge separation $L = 100$ mm

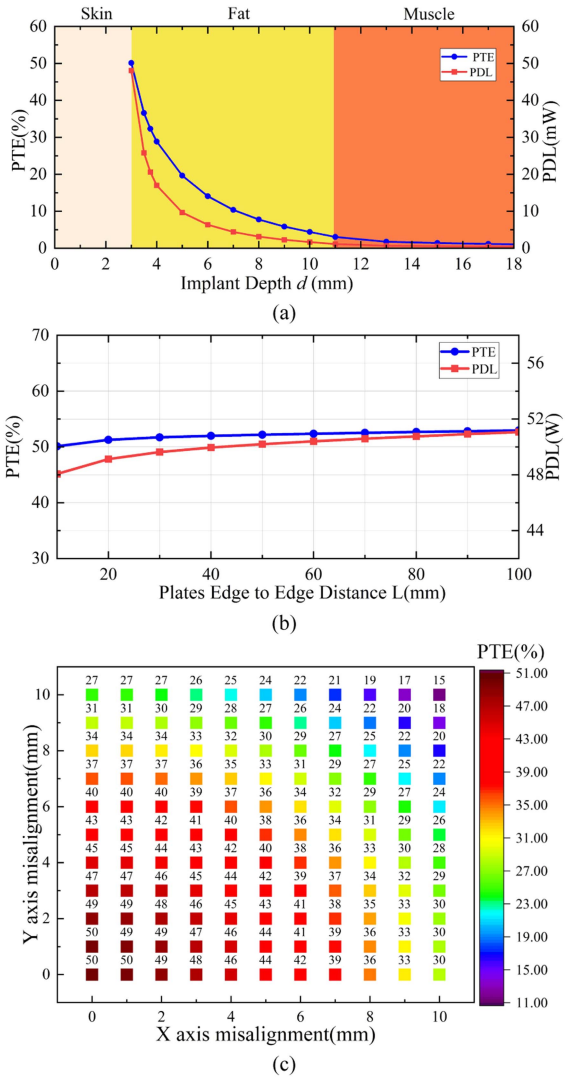

Fig. 10. Simulation results of PTE and PDL as a function of (a) implant depth, (b) edge-to-edge separation L, and (c) X- and Y-axis misalignment at 3-mm implant depth.

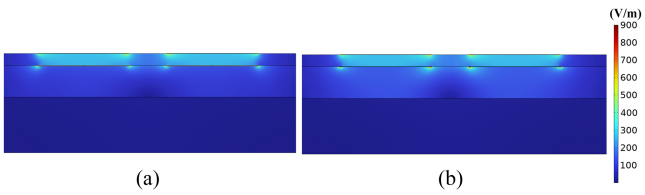

Fig. 11. Electric field distribution of (a) asymmetric insulation implants and (b) symmetric insulation implants.

(PTE = 52.96% and PDL = 51.07 mW). The lowest PTE and PDL are obtained when $L = 1$ cm (PTE = 50.12% and PDL = 48.06 mW). As L increases, the PTE increases by less than 2.84%, and the PDL increases less than 3.01 mW. Therefore, a small L can also maintain a considerable PTE and PDL.

In practical applications, misalignment between the Tx and Rx plates is inevitable due to human movement. Therefore, Fig. 10(c) depicts the simulation results for misalignments between 0 and 10 mm in the X-axis and Y-axis at 3-mm implant depth. The results indicate that an efficiency of over 38% can be maintained when $X = 5$ mm and $Y = 5$ mm. However, only 30% and 27% efficiency can be achieved when $X = 10$ mm and $Y = 10$ mm, respectively. This shows that the system misalignment tolerance is not good enough. Furthermore, a larger area of the Tx plate can be used to increase the misalignment tolerance, which will be discussed in Section IV-C.

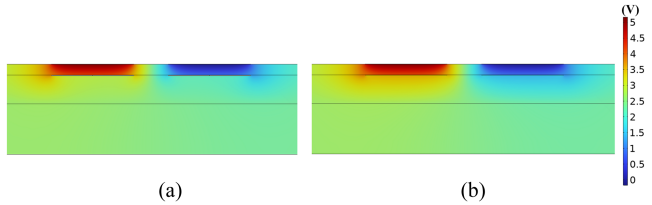

Fig. 12. Electric potential distribution of (a) asymmetric insulation implants and (b) symmetric insulation implants.

IV. Safety Assessment

In the previous section, the coupler is designed, and the structure of the asymmetric insulation layer is presented. In this section, SAR and temperature field safety assessments are performed for asymmetric and symmetric insulations. Furthermore, the strategy to improve the energy transfer capability and miniaturize the Rx components within the safety constraints of SAR is investigated.

A. SAR Assessment

IEEE C95.1 [34] guideline identifies two primary safety concerns for human exposure to RF electromagnetic fields: tissue thermal effects limited by SAR from 100 kHz to 300 GHz and electrostimulation limited by electric fields in the frequency range of 0 Hz to 5 MHz. According to the guideline, only SAR limits apply for the 6.78-MHz operating frequency. The restriction of maximum local SAR averaged over any 10 g of tissue in the shape of a cube is limited to 2 W/kg. SAR can be correlated to E_{rms} at a point in the body by

$$\mathrm{SAR} = \frac{\sigma |E_{\mathrm{rms}}|^2}{\rho} \tag{16}$$

where σ is the conductivity of human tissue in S/m, ρ is the density of human tissue in kg/m^3, and E_{rms} is the root-mean-square electric field strength of tissue in V/m. The local SAR averaged per 10 g of tissue is calculated according to the guidelines [34], [35], which is a volume average of SAR at each grid point within an equilateral length cube of mass 10 g. COMSOL is used for safety assessment, and the electric field and electric potential distribution simulation results for symmetric insulation and asymmetric insulation implants at a safety limit of 2 W/kg are shown in Figs. 11 and 12.

Fig. 13 demonstrates the PDL for the symmetric insulation ($t_2 = 0.015$ mm) and asymmetric insulation ($t_2 = 0.15$ mm) implants with an average SAR of 2 W/kg as safety limitation. For asymmetric insulation implants, 64.67 mW is transmitted at 50.12% PTE, and for implants with symmetric insulation,

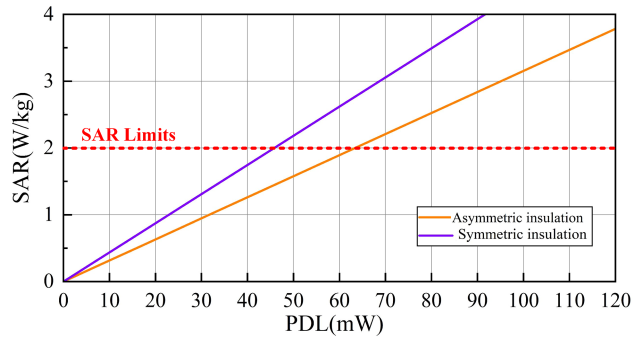

Fig. 13. Simulation results of SAR versus PDL at $R = r = 11.28$ mm.

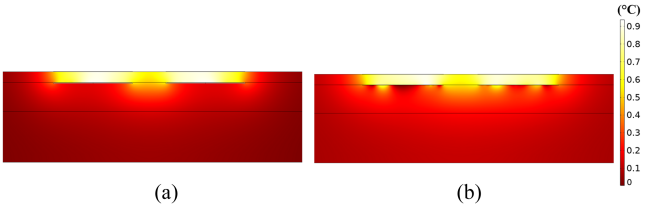

Fig. 14. Temperature rise distribution of (a) asymmetric insulation implants and (b) symmetric insulation implants.

47.01 mW of energy is safely transmitted at 43.07% PTE. Asymmetric structures can transmit around 37.56% extra energy compared with symmetric structures, which is a great enhancement for transmission capacity.

B. Temperature Field Evaluation

The temperature increase of tissue is also a part of the safety assessment; literatures [36] and [37] demonstrate that the thermal tolerance limit of the skin for long duration of time is 41.8°C °C and will cause damage or pain to the human body when reaching 42°C–45 °C. With the initial human body temperature set at 36.5 °C, Fig. 14 displays the temperature increase distribution of asymmetric insulation and symmetric insulation implants that are wirelessly charged for 1 h at 64.67- and 47.01-mW PDL, respectively. The results show a maximum temperature rise of 0.93 ° and 0.90 °C, which is in compliance with biosafety specifications.

C. Power Transfer Strategy in SAR Limits.

In this section, the strategies to improve PDL, misalignment tolerance, and implant miniaturization under SAR safety constraints by varying the radius of Tx and Rx plates are investigated for asymmetric insulation implants ($t_1 = 0.015$ mm and $t_2 = 0.15$ mm). Set the radius of the Tx plates as $R = r_1 \times 11.28$ mm ($1 \le r_1 \le 1.8$) and the radius of Rx plates as $r = r_2 \times 11.28$ mm ($0.2 \le r_2 \le 1$), where r_1 and r_2 as the radius factors. Edge-to-edge distance L maintains 10 mm.

Fig. 15 shows the maximum PDL at different Tx and Rx sizes at an average SAR limit of 2 W/kg, and each data point has tracked to its optimum PTE load. It can be found that increasing the Tx radius R improves the PDL, and the PDL increases rapidly with r_1 when $1 \le r_1 \le 1.4$, and the growth rate slows down

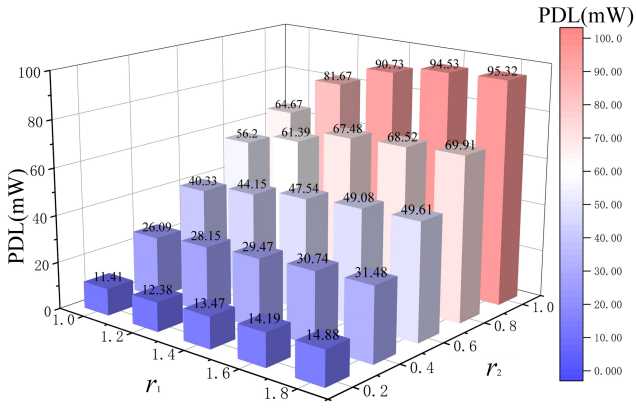

Fig. 15. PDL with different TX and RX sizes under SAR (2 W/kg) constraints.

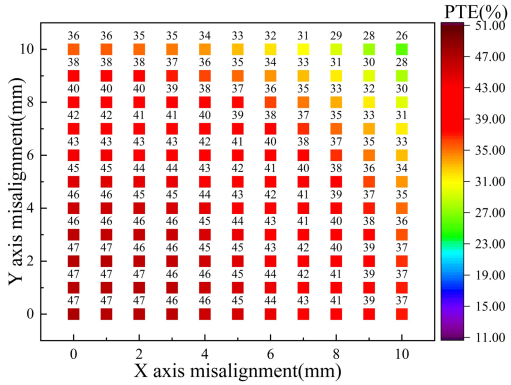

Fig. 16. Simulation results of PTE as a function of X- and Y-axis misalignment at r_1: $r_2 = 1.4$:1.

when $1.4 \le r_1 \le 1.8$. With r_1:$r_2 = 1.4$:1, 90.73 mW PDL can be safely transferred, which is 26.06 mW more compared to r_1:$r_2 = 1$:1. The Rx radius r has a significant effect on the PDL, which decreases as the PDL decrease. However, a sizable PDL can still be maintained with a larger Tx radius, which provides a strategy for implant miniaturization. When r_1:$r_2 = 1.4$:0.8, 67.48 mW PDL is safely delivered, which is 2.81 mW more compared to r_1:$r_2 = 1$:1; meanwhile, the Rx is only 64% of the original area. As r_2 continues to decrease, the improvement by increasing r_1 decreased significantly. Therefore, r_1:$r_2 = 1.4$:0.8 is chosen as an optional strategy for miniaturization.

Fig. 16 shows the misalignment tolerance for r_1:$r_2 = 1.4$:1, which has a 3% reduction in efficiency when $X = Y = 0$ but significantly improves the overall system misalignment tolerance compared to r_1:$r_2 = 1$:1 in Fig. 10. Larger Tx radius reduces the transverse impedance $Z_{1,2,3,4S}$, longitudinal impedance Z_S, and bypass impedance Z_{sf}, thus causing an increase in PDL and reduction in PTE. Large PDL and excellent misalignment tolerance simultaneously achieved at 1.4:1.

V. Experimental Verification

A. Experimental Setup

To validate the accuracy of the proposed transcutaneous CPT model and the superiority of the designed coupler, an

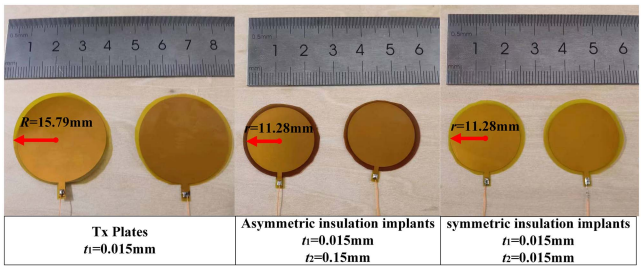

Fig. 17. Photograph of the Tx plates and implanted Rx plates with the coated Kapton insulation film.

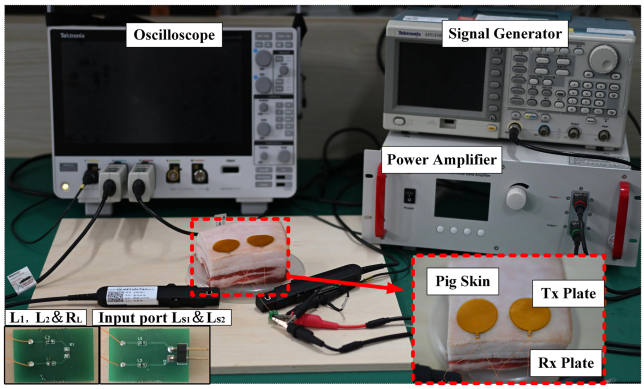

Fig. 18. Photograph of the transcutaneous CPT prototype.

TABLE III
SYSTEM PARAMETER VALUE

Parameter	Value	Parameter	Value
U_{in}	6.1 V	$C_{1,3}$	853 pF
f	6.78 MHz	t_1	0.015 mm
$L_{S1,2}$	330 nH	t_2	0.015 mm, 0.15 mm
$L_{1,2}$	820 nH	R	15.79 mm
$C_{S1,2}$	1696 pF	r	11.28 mm

experimental test is conducted using pork. For a better match between the experimental results and the simulation results, the pork is prepreserved in the thermostat to keep it at 36.5 °C. Flexible copper foils of 0.01 mm thickness are coated with Kapton insulating film, and Rx plates are divided into two groups of symmetric insulation ($t_1 = 0.015$ mm and $t_2 = 0.015$ mm) and asymmetric insulation ($t_1 = 0.015$ mm and $t_2 = 0.15$ mm), as shown in Fig. 17. The Tx plates ($R = 1.4\times11.28$ mm) are placed in contact with the skin of the pork, and then, the Rx plates ($r = 11.28$ mm) are inserted underneath the 3.2 mm-thick skin through a thin incision. The experimental setup is shown in Fig. 18.

As MRI compatibility is often a requirement for transcutaneous implants, RF inductors (TDK MLF series) with 1.2 mg weight ferrite are used to compensate the circuit, which will not pose as a hazard to MRI patients implanted with the device. The value of the inductors is calculated by (5) and (6) based on the capacitance of the insulating layer obtained from the impedance analyzer (Keysight E4990A). The signal generator (Tektronix AFG3102C) drives the wideband amplifier (Aigtek ATA-1220E), producing a sinusoidal voltage U_{in} of 6.1 V_p at the

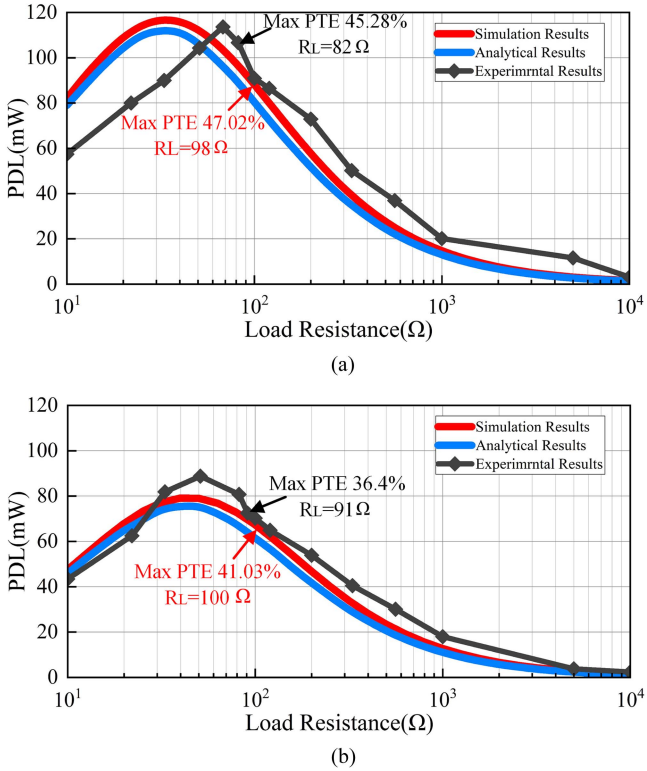

Fig. 19. Experimental, simulation, and analytical results of (a) PDL versus R_L for the coupler with asymmetric insulation ($t_1 = 0.015$ mm and $t_2 = 0.15$ mm). (b) PDL versus R_L for the coupler with symmetric insulation ($t_1 = 0.015$ mm and $t_2 = 0.015$ mm).

Tx side. The voltage U_{in} and current I_{in} and I_{out} are measured using the oscilloscope (Tektronix MDO34). Differential probes are used to eliminate the loop coupling formed between the power amplifier and the oscilloscope through the ground. Then, the PTE and PDL are calculated according to (12), (13), and (14). The system specifications are listed in Table III.

B. Simulation and Experimental Results

Fig. 19 depicts the PDL for two sets of comparison experiments when the load is increased from 10 to 10 000 Ω. In both the sets of data, the simulated results in red are generally in agreement with the analytical results in blue. The experimental results in black show a slight deviation from both the simulation and analytical results. The maximum PTE simulation for asymmetric insulation is 47.02% ($R_L = 98$ Ω), and experiment is 45.28% ($R_L = 82$ Ω), maximum PDL simulation is 116.51 mW ($R_L = 32$ Ω), and experiment is 113.6 mW ($R_L = 68$ Ω). For symmetric insulation, the maximum simulated PTE value is 41.03% ($R_L = 100$ Ω), while the experimental value is 36.4% ($R_L = 91$ Ω), and the maximum simulated PDL value is 79.13 mW ($R_L = 40$ Ω), while the experimental value is 88.78 mW ($R_L = 51$ Ω). The maximum PTE of the asymmetric insulation is enhanced by approximately 8.9%, and the PDL was enhanced by about 24.8 mW compared to the symmetric insulation layer.

It can be observed that for both the sets of results, the loads R_L of maximum PTE and maximum PDL obtained by the

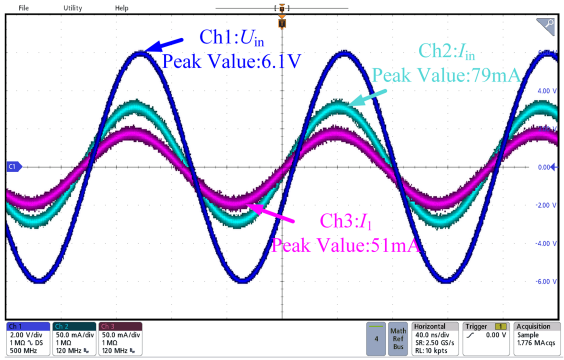

Fig. 20. Waveforms of the asymmetric insulation coupler when $R_L = 82\ \Omega$.

TABLE IV
COMPARISONS BETWEEN RECENT WORKS

	[12]	[40]	[23]	This work
WPT method	IPT	IPT	Nonresonant CPT	Resonant CPT
Medium	Air	Pig	Pig skin	pork
Depth	10 mm	50 mm	5 mm	3 mm
Frequency	1 MHz	40.68 MHz	442.4 MHz	6.78 MHz
Rx Size	Diameter 20 mm	Diameter 14 mm	One pair of 900 mm^2	Two pairs of 400 mm^2
PTE (AC-AC)	41.2%	0.27%	50.4%	47.02%
PDL	–	5.4 mW	71.3 mW	90.73 mW

experiment are much closer to each other, whereas R_L of maximum PTE and PDL obtained by the simulation and the theoretical analysis is somewhat different. Also, we can observe that the PTE achieved by the experiment is about 2–5% smaller compared to the simulation and analysis. The difference mentioned earlier is caused partly by the internal resistance of the wire and the compensating inductors and mainly by the difference in dielectric properties between pork tissue and human tissue. Meanwhile, the dielectric properties of pork vary with storage time, freshness, temperature, etc., and these factors ultimately lead to some load shift and efficiency reduction in experimental results. However, the two sets of experimental results still illustrate the accuracy of modeling and the superiority of the coupler design. The waveforms of the input voltage, current, and output current are measured when $R_L = 82\ \Omega$ for asymmetric insulation implants, as shown in Fig. 20. It is noted that the input current in green is 12.2° ahead of the input voltage in blue, which indicates that the link exhibits capacitive.

C. Comparison With Recent Works

Table IV shows a comparison with recent work. IPT has great success in powering moderate of power to deep implants. CPT is more suitable for delivering 70–100 mW of energy for implants less than 5 mm depth due to its smaller EMI. Compared to nonresonant CPT [23], the implant depth in our work is shallower, but it can transfer more energy to the load under the limitation of SAR = 2 W/kg, and the efficiency of the rectifier will be improved at 6.78 MHz compared to hundreds of megahertz. Limited by energy transfer depth, the coupler designed in this article is suitable for powering subcutaneous implants, such as glucose and enzyme detectors [38], or powering the device via biocompatible wire. The wire between the device and the coupler avoids individual fat layer differences but introduces the risk of infection. Literature [39] suggested that the use of antibiotics prior to implantation had a protective effect. Future work will focus on optimizing the coupler to minimize the risk of infection and designing the high-efficiency rectifier.

VI. CONCLUSION

In this article, the design of a human implantable resonant CPT system with flexible thin-film electrodes is presented. The accurate circuit model with multilayer tissue is proposed to identify key influences on PDL versus PTE and then verified by COMSOL simulation and experiment. A prototype system with the asymmetric insulation structure is built, and 90.73 mW of energy is delivered at 47.02% efficiency within the limits of IEEE safety guidelines. In addition, the system is insensitive to edge-to-edge separation and has good misalignment tolerance, which is helpful for practical application.

REFERENCES

[1] J. M. Khalifeh et al., "Electrical stimulation and bone healing: A review of current technology and clinical applications," *IEEE Rev. Biomed. Eng.*, vol. 11, pp. 217–232, 2018.
[2] C.-Y. Tsui and W.-H. Ki, "Energy harvesting and power delivery for implantable medical devices," *Found. Trends Electron. Des. Automat.*, vol. 7, no. 3, pp. 179–246, 2013.
[3] J. Charthad et al., "An ultrasonically powered implantable device for targeted drug delivery," in *Proc. 38th Annu. Int. Conf. IEEE Eng. Med. Biol. Soc.*, 2016, pp. 541–544.
[4] J. Yoo, L. Yan, S. Lee, Y. Kim, and H.-J. Yoo, "A 5.2 mW self-configured wearable body sensor network controller and a 12 μW wirelessly powered sensor for a continuous health monitoring system," *IEEE J. Solid-State Circuits*, vol. 45, no. 1, pp. 178–188, Jan. 2010.
[5] M. W. Baker, "A low-power cochlear implant system," Ph.D. dissertation, Dept. Elect. Eng. Comput. Sci., Massachusetts Inst. Technol., Cambridge, MA, USA, 2007.
[6] Y. -K. Lo, K. Chen, P. Gad, and W. Liu, "A fully-integrated high-compliance voltage SoC for epi-retinal and neural prostheses," *IEEE Trans. Biomed. Circuits Syst.*, vol. 7, no. 6, pp. 761–772, Dec. 2013.
[7] S. Roy, A. N. M. W. Azad, S. Baidya, M. K. Alam, and F. Khan, "Powering solutions for biomedical sensors and implants inside the human body: A comprehensive review on energy harvesting units, energy storage, and wireless power transfer techniques," *IEEE Trans. Power Electron.*, vol. 37, no. 10, pp. 12237–12263, Oct. 2022.
[8] K. Agarwal, R. Jegadeesan, Y.-X. Guo, and N. V. Thakor, "Wireless power transfer strategies for implantable bioelectronics," *IEEE Rev. Biomed. Eng.*, vol. 10, pp. 136–161, 2017.
[9] R. G. Hauser, "The growing mismatch between patient longevity and the service life of implantable cardioverter-defibrillators," *J. Amer. College Cardiol.*, vol. 45, no. 12, pp. 2022–2025, 2005.
[10] M. Meng and M. Kiani, "Design and optimization of ultrasonic wireless power transmission links for millimeter-sized biomedical implants," *IEEE Trans. Biomed. Circuits Syst.*, vol. 11, no. 1, pp. 98–107, Feb. 2017.
[11] R. H. Caverly, "Breakthroughs in microwaves: Increasing signal strength in swarms of wireless sensors—An interview with Dr. Aydin Babakhani," *IEEE J. Microw.*, vol. 1, no. 2, pp. 532–539, Apr. 2021.
[12] U.-M. Jow and M. Ghovanloo, "Design and optimization of printed spiral coils for efficient transcutaneous inductive power transmission," *IEEE Trans. Biomed. Circuits Syst.*, vol. 1, no. 3, pp. 193–202, Sep. 2007.
[13] M. Kiani, U.-M. Jow, and M. Ghovanloo, "Design and optimization of a 3-coil inductive link for efficient wireless power transmission," *IEEE Trans. Biomed. Circuits Syst.*, vol. 5, no. 6, pp. 579–591, Dec. 2011.

[14] M. Kováč, V. Stopjaková, D. Arbet, L. Nagy, and J. Brenkuš, "Investigation of on-chip coil in 130 nm standard CMOS for WPT and bio-applications," in *Proc. Int. Conf. Emerg. eLearn. Technol. Appl.*, 2016, pp. 177–182.
[15] M. A. Callejón, J. Reina-Tosina, D. Naranjo-Hernández, and L. M. Roa, "Galvanic coupling transmission in intrabody communication: A finite element approach," *IEEE Trans. Biomed. Eng.*, vol. 61, no. 3, pp. 775–783, Mar. 2014.
[16] B. Kibret, M. Seyedi, D. T. H. Lai, and M. Faulkner, "Investigation of galvanic-coupled intrabody communication using the human body circuit model," *IEEE J. Biomed. Health Informat.*, vol. 18, no. 4, pp. 1196–1206, Jul. 2014.
[17] P. Chen, H. Yang, R. Luo, and B. Zhao, "A tissue-channel transcutaneous power transfer technique for implantable devices," *IEEE Trans. Power Electron.*, vol. 33, no. 11, pp. 9753–9761, Nov. 2018.
[18] M. A. Rothfuss et al., "Implantable energy harvesting stents for transcutaneous wireless monitoring of peripheral artery disease," *IEEE Sens. J.*, vol. 18, no. 5, pp. 2077–2090, Mar. 2018.
[19] J. Minguillon et al., "Powering electronic implants by high frequency volume conduction: In human validation," *IEEE Trans. Biomed. Eng.*, vol. 70, no. 2, pp. 659–670, Feb. 2023.
[20] R. Sedehi et al., "A wireless power method for deeply implanted biomedical devices via capacitively coupled conductive power transfer," *IEEE Trans. Power Electron.*, vol. 36, no. 2, pp. 1870–1882, Feb. 2021.
[21] R. Jegadeesan, K. Agarwal, Y.-X. Guo, S.-C. Yen, and N. V. Thakor, "Wireless power delivery to flexible subcutaneous implants using capacitive coupling," *IEEE Trans. Microw. Theory Techn.*, vol. 65, no. 1, pp. 280–292, Jan. 2017.
[22] M. Tamura, Y. Naka, K. Murai, and T. Nakata, "Design of a capacitive wireless power transfer system for operation in fresh water," *IEEE Trans. Microw. Theory Techn.*, vol. 66, no. 12, pp. 5873–5884, Dec. 2018.
[23] T. Segawa, R. Aoyama, and M. Tamura, "Electrode design theory using highly accurate equivalent circuits in biological capacitive WPT," *IEEE Microw. Wireless Technol. Lett.*, vol. 33, no. 6, pp. 943–946, Jun. 2023.
[24] M. Tamura, K. Murai, and M. Matsumoto, "Design of disposable film-type capacitive wireless charging for implantable medical devices," in *Proc. IEEE MTT-S Int. Microw. Symp.*, 2021, pp. 58–61.
[25] M. Tamura, T. Segawa, and M. Matsumoto, "Capacitive coupler for wireless power transfer to intravascular implant devices," *IEEE Microw. Wireless Compon. Lett.*, vol. 32, no. 6, pp. 672–675, Jun. 2022.
[26] R. Erfani, F. Marefat, A. M. Sodagar, and P. Mohseni, "Transcutaneous capacitive wireless power transfer (C-WPT) for biomedical implants," in *Proc. IEEE Int. Symp. Circuits Syst.*, 2017, pp. 1–4.
[27] R. Erfani, F. Marefat, A. M. Sodagar, and P. Mohseni, "Modeling and experimental validation of a capacitive link for wireless power transfer to biomedical implants," *IEEE Trans. Circuits Syst. II, Exp. Briefs*, vol. 65, no. 7, pp. 923–927, Jul. 2018.
[28] A. N. M. S. Hossain, R. Erfani, P. Mohseni, and H. M. Lavasani, "On the non-idealities of a capacitive link for wireless power transfer to biomedical implants," *IEEE Trans. Biomed. Circuits Syst.*, vol. 15, no. 2, pp. 314–325, Apr. 2021.
[29] A. N. M. S. Hossain, P. Mohseni, and H. M. Lavasani, "Design and optimization of capacitive links for wireless power transfer to biomedical implants," *IEEE Trans. Biomed. Circuits Syst.*, vol. 16, no. 6, pp. 1299–1312, Dec. 2022.
[30] R. E. De Filippo and A. Atala, "Stretch and growth: The molecular and physiologic influences of tissue expansion," *Plast. Reconstructive Surg.*, vol. 109, no. 7, pp. 2450–2462, 2002.
[31] C. Gabriel, S. Gabriel, and Y. E. Corthout, "The dielectric properties of biological tissues: I. Literature survey," *Phys. Med. Biol.*, vol. 41, no. 11, 1996, Art. no. 2231.
[32] S. Gabriel, R. W. Lau, and C. Gabriel, "The dielectric properties of biological tissues: II. Measurements in the frequency range 10 Hz to 20 GHz," *Phys. Med. Biol.*, vol. 41, no. 11, 1996, Art. no. 2251.
[33] S. Gabriel, R. W. Lau, and C. Gabriel, "The dielectric properties of biological tissues: III. Parametric models for the dielectric spectrum of tissues," *Phys. Med. Biol.*, vol. 41, no. 11, 1996, Art. no. 2271.
[34] *IEEE Standard for Safety Levels With Respect to Human Exposure to Electric, Magnetic, and Electromagnetic Fields, 0 Hz to 300 GHz*, IEEE Standard C95. 1-2019 (Revision of IEEE Standard C95. 1-2005/Incorporates IEEE Standard C95. 1-2019/Cor 1-2019), Oct. 2019, pp. 1–312.
[35] *Determining the Peak Spatial-Average Specific Absorption Rate (SAR) in the Human Body From Wireless Communications Devices, 30 MHz to 6 GHz—Part 1: General Requirements for Using the Finite-Difference Time-Domain (FDTD) Method for SAR Calculations*, Standard IEC/IEEE 62704-1:2017, 2017, pp. 1–86.
[36] J. M. Bull et al., "Whole body hyperthermia: A phase-l trial of a potential adjuvant to chemotherapy," *Ann. Intern. Med.*, vol. 90, no. 3, pp. 317–323, 1979.
[37] H. S. Sharma and P. J. Hoopes, "Hyperthermia induced pathophysiology of the central nervous system," *Int. J. Hyperthermia*, vol. 19, no. 3, pp. 325–354, 2003.
[38] Y. J. Heo, H. Shibata, T. Okitsu, and S. Takeuchi, "Long-term in vivo glucose monitoring using fluorescent hydrogel fibers," *Proc. Nat. Acad. Sci.*, vol. 108, no. 33, pp. 13399–13403, 2011.
[39] M. R. Sohail et al., "Risk factor analysis of permanent pacemaker infection," *Clin. Infect. Dis.*, vol. 45, no. 2, pp. 166–173, 2007.
[40] I. Habibagahi, J. Jang, and A. Babakhani, "Miniaturized wirelessly powered and controlled implants for multisite stimulation," *IEEE Trans. Microw. Theory Techn.*, vol. 71, no. 5, pp. 1911–1922, May 2023.

Chunwei Cai (Member, IEEE) was born in Shandong Province, China, in 1977. He received the B.S. and M.S. degrees in control theory and control engineering from Shan Dong University, Jinan, China, in 2001 and 2004, respectively, and the Ph.D. degree in electrical engineering from the Harbin Institute of Technology (HIT), Harbin, China, in 2013.

Since 2006, he has been a Lecturer with HIT, Weihai, China, where he has also been a Professor since 2014. His current research interests include wireless power transfer systems, power converters, and inverters.

Tian Chen was born in Hubei Province, China, in 2000. He received the B.S. degree in electrical engineering in 2022 from the Harbin Institute of Technology, Weihai, China, where he is currently working toward the M.S. degree in electrical engineering.

His current research interests include power electronics and wireless power transfer systems for implanted biomedical devices.

Xiuyun Ren received the B.A. degree in physics and the M.S. degree in optics from Shandong Normal University, Jinan, China, in 2002 and 2005, respectively, and the Ph.D. degree in physical electronics from the Harbin Institute of Technology, Harbin, China, in 2016.

Since 2014, she has been an Associate Professor with the School of Information Science and Engineering, Harbin Institute of Technology, Weihai, China. Her research interests include Lidar ocean exploration, wireless communication technology, and optoelectronic technology, and their applications.

Yujie Jiao was born in Shanxi Province, China, in 2001. He received the B.S. degree in electrical engineering from the Wuhan University of Technology, Wuhan, China, in 2023. He is currently working toward the M.S. degree in electrical engineering with the Harbin Institute of Technology, Weihai, China.

His current research interests wireless power transfer systems for implanted biomedical devices.

Xichen Liu (Student Member, IEEE) was born in Shandong Province, China, in 1998. He received the B.S. and M.S. degrees in electrical engineering in 2020 and 2023, respectively, from the Harbin Institute of Technology, Weihai, China, where he is currently working toward the Ph.D. degree in electrical engineering.

His current research interests include power electronics and wireless power transfer systems for autonomous underwater vehicles and unmanned aerial vehicles.

Chenghao Li (Student Member, IEEE) was born in Liaoning Province, China, in 2000. He received the B.S. degree in electrical engineering in 2023 from the Harbin Institute of Technology, Weihai, China, where he is currently working toward the Ph.D. degree in electrical engineering.

His current research interests include long-distance seawater capacitive power transfer, mechanism of electromagnetic field, and simultaneous wireless power and data transfer.

Jinpeng Yu (Senior Member, IEEE) received the B.Sc. degree in automation from Qingdao University, Qingdao, China, in 2002, the M.Sc. degree in system engineering from Shandong University, Jinan, China, in 2006, and the Ph.D. degree in system theory from the Institute of Complexity Science, Qingdao University, Qingdao, in 2011.

He is currently a Distinguished Professor with the School of Automation, Qingdao University. His research interests include electrical energy conversion and motor control, applied nonlinear control, and intelligent systems.

Dr. Yu is a recipient of the Shandong Province Taishan Scholar Special Project Fund and Shandong Province Fund for Outstanding Young Scholars. He was an Associate Editor for several journals, including IEEE TRANSACTIONS ON CYBERNETICS, IEEE TRANSACTIONS ON NEURAL NETWORKS AND LEARNING SYSTEMS, IEEE TRANSACTIONS ON CIRCUITS AND SYSTEMS—PART I: REGULAR PAPERS, IEEE TRANSACTIONS ON CIRCUITS AND SYSTEMS—PART II: EXPRESS BRIEFS, *Information Sciences*, *Journal of the Franklin Institute*, *ISA Transactions*, and *Journal of System Science and Complexity*.

Shuai Wu (Member, IEEE) was born in Shanxi Province, China, in 1995. He received the B.S. degree in electrical engineering and automation from Shanxi Agricultural University, Jinzhong, China, in 2017, and the M.S. and Ph.D. degrees in electrical engineering from the Harbin Institute of Technology (HIT), Harbin, China, in 2019 and 2023, respectively.

Since 2023, he has been an Associate Professor with the School of New Energy, HIT, Weihai, China. His current research interests include wireless power transfer for unmanned vehicles and implanted biomedical devices.